PCCP

Study of Decahedral Multimetallic Nanoparticles Using Large-Angle Convergent-Beam Electron Diffraction

Journal:	*Physical Chemistry Chemical Physics*
Manuscript ID	CP-ART-01-2025-000109.R2
Article Type:	Paper
Date Submitted by the Author:	22-Mar-2025

Complete List of Authors:	Rogers, Blake; Champion Fiberglass Inc, Research and Developoment Rufino da Silva, Carlos; Northern Arizona University, Applied Physics and Materials Science Palomares Báez, Juan Pedro; Universidad Autónoma de Chihuahua Facultad de Ciencias Químicas Velazquez-Salazar, Jesus; Northern Arizona University, Applied Physics and Materials Science Rodríguez-López, José; Circ. Paseo de los Pinos , Montejano-Carrizales, Juan; Universidad Autonoma de San Luis Potosi, Instituto de Física Yacaman, Miguel; Northern Arizona University, APMS

PCCP

ARTICLE TYPE

Cite this: DOI: 00.0000/xxxxxxxxxx

Study of Decahedral Multimetallic Nanoparticles Using Large-Angle Convergent-Beam Electron Diffraction

Blake Rogers,[ab] Carlos E. Rufino da Silva,*[a] Juan Pedro Palomares-Báez,*[c] J. Jesús Velázquez Salazar,[a] José Luis Rodríguez López,[d] Juan Martín Montejano-Carrizales,[e] and Miguel José Yacamán[a]

Received Date
Accepted Date

DOI: 00.0000/xxxxxxxxxx

In this work, we characterize AuCuNiPd decahedral nanoparticles using advanced electron microscopy and computational techniques. Additionally, we introduce a novel method for analyzing asymmetrical HOLZ patterns, enabling highly precise lattice spacing determinations. By combining convergent beam electron diffraction (CBED) imaging with molecular dynamics simulations, we gain valuable insights into the structural properties of these nanoparticles. Our results reveal a globally distorted FCC lattice, best approximated by a body-centered tetragonal (BCT) structure with lattice parameters a = b = 0.287 nm and c = 0.415 nm. From LACBED analysis, the strain distribution in decahedra consists of two pairs of tetrahedra with distinct strain values, while the fifth tetrahedron exhibits a unique strain state.

1 Introduction

Decahedral nanoparticles of noble metals have fascinated researchers for almost half a century. Since their discovery by Ino [1] more than 300 papers has been published about this topic. One of the key aspects of decahedral particles arises from the fact that five tetrahedra arranged to create a decahedron will leave a gap of 7.36 degrees. Thus, in the growth process of decahedral nanoparticles, to compensate for this geometric mismatch, the structure must undergo a distortion, leading to an overall strained configuration. Two main models have been presented based in homogeneous [2,3] or inhomogeneous strain [4,5]. However, the distinction between those mechanisms is very difficult to establish. As recently mentioned, the strain in general will contain homogeneous and inhomogeneous component and any diffraction experiment probes the average value over the volume of the illuminated region. As a consequence the inhomogeneous components vary both in magnitude and sign from point to point, so the leading term is always the homogeneous component [5]. Some research using High-Resolution Electron Microscopy (HREM) and the Geometric Phase Analysis (GPA) method [6,7] suggest that, in the case of gold, the strain distribution might be more complicated since the measured rotation components do not add to the expected 7.36°.

The reported work has been made for single or bimetallic particles. In the modern materials science, the multimetallic alloys play an important role. New alloys are made leaving the traditional ones, in which one component is dominant, to produce alloys with 4 or 5 metals with similar concentrations. Examples of those alloys are the High-Entropy Alloys (HEA) [8,9], Heusler alloys [10–12] and Quasicrystals [13,14]. Multimetallic nanoparticles (MMNP) are of high importance in fields such as catalysis [11,15] and additive manufacturing of HEA [16,17]. The MMNP have enhanced properties and might help to solve some of the most pressing problems in cleaning the environment by substituting of noble metals in many energy generation reactions [18] and in environmental control [19].

Recently, Nelly *et al.* [20], reviewed the main sources of strain in alloy nanoparticles, which include finite size effects, morphology, domain structure, i.e., the arrangement of different phases within a nanoparticle can induce strain; lattice mismatch and chemical ordering. These sources of strain can lead to complex distributions within nanoparticles, impacting their structural and functional properties significantly.

To study strain in solids one of the most useful techniques is the Large-Angle Convergent Beam Electron Diffraction (LACBED) [21,22], it has been successfully used in semiconductor and metallurgical research [23,24], and to determine strain in devices, epitaxial structures, *etc.* [25–28] In the present work we used LACBED to study decahedral nanoparticles of AuCuNiPd prepared

[a] *Department of Applied Physics and Materials Science, Northern Arizona University, Flagstaff, AZ, 86011, USA.; E-mail: carloseduardorufino7@gmail.com, and ppalomares@uach.mx*
[b] *Present address: Champion Fiberglass Inc, Research and Developoment, 6400 Spring Stuebner Road Spring, TX, 77389, USA.*
[c] *Facultad de Ciencias Químicas, Universidad Autónoma de Chihuahua, Chihuahua, Mexico 31125.*
[d] *Jardines de Jacarandas, 78136, San Luis Potosí, SLP MX.*
[e] *Instituto de Física, Universidad Autónoma de San Luis Potosí, San Luis Potosí, Mexico 78290.*

with similar concentrations. This case is particularly interesting because it has an extra degree of freedom which is produced by the differences in atomic radius of the components. This adds complexity with respect to the case of single metal nanoparticles. In the case of the bulk multimetallic alloys it is assumed that because the atomic radius differences a local strain is present along the alloy that will eventually stop dislocation movement[29]. However, as discussed by Owen[30], this assumption has never been experimentally proven. Therefore, studying multimetallic nanoparticles (MMNPs) with twin boundaries may provide new insights to this phenomenon[31].

2 Particle characterization and theoretical calculations

AuCuNiPd nanoparticles were synthesized using a thermal decomposition method. In a 20 mL glass vial, 7 mL of OLA was heated to 120 °C for 10 min with stirring magnet. Then 100 μL of $HAuCl_4$ (0.1 M), 100 μL of $CuCl_2$ (0.1 M), 100 μL NiCl (0.1 M), and 100 μL PdCl (0.1 M, all stok solutions were prepared in ethanol) were sequentially injected into heated oleylamine drop by drop using syringes, and the mixture was stirred for 7 min at 120 °C. After, the temperature was increased to 280 °C. During this process the color of the solution changed to black color. Then, the solution was removed from the heat source and cooled to room temperature. The solution was washed with acetone/ethanol three times by centrifugation and dispersed with chloroform, with a final metal concentration of 25 wt%. The detailed methodology is described by Velázquez Salazar *et al.*[32]. We characterized the nanoparticles by using a TEM Talos 200i from Thermo Fischer. The chemical analysis was performed using dispersive X-ray spectroscopy (EDS) together with High-Angle Annular Dark-Field Scanning Transmission Electron Microscopy (HAADF-STEM) images. We studied the nanoparticle using two main diffraction techniques, both based on convergent beam electron diffraction[33]. In particular we apply High Order Laue Zone patterns (HOLZ) and Large Angle Convergent Beam Electron Diffraction (LACBED)[34–36]. Most of shapes of the fabricated nanoparticles correspond to regular and irregular decahedron, triangiular, and isosahedral. The average size of the nanoparticles is around 60 nm, and most of the particles are pentagonal. This was demonstrated using HAADF-STEM thickness profile which do not show small varaitions along the nanoparticle as shown in Figure 1. The average composition of the nanoparticles studied in this paper was determined by EDS in the TEM. The resulting composition an was Au 61.63, Cu 26.35, Pd 10.7, and Ni 1.14. Despite of using equal concentrations of the metals during the synthesis, the final composition of the nanoparticles is not the same as the initial concentration. That is the result of the differences on kinetics reduction of the different metal salts. This results in a distribution of concentrations. We selected the above mentioned coimposition because around 70% of the particles show this metal distribution. The EDS results are shown in Figure 2.

To simulate and optimize the chemical order of these species, a hybrid molecular dynamics (MD) and Monte Carlo (MC) method

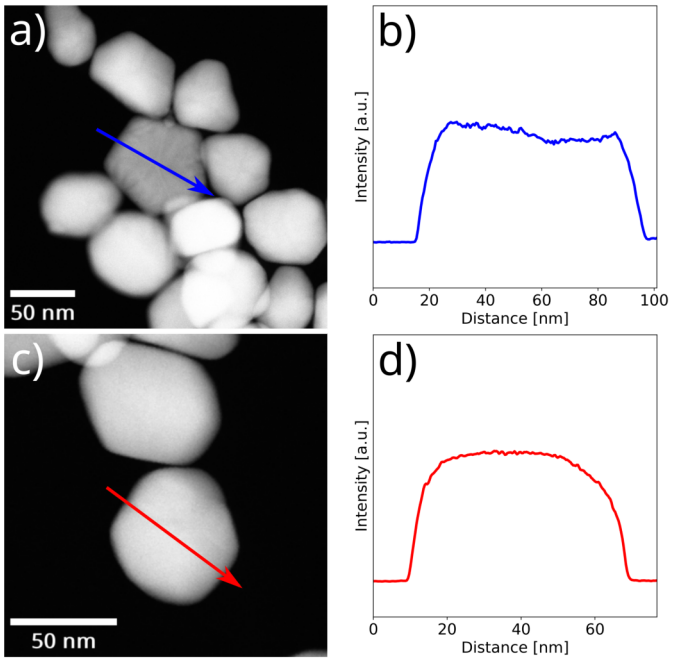

Fig. 1 HAADF-STEM images of the produced AuCuNiPd nanoparticles. A decahedron structure is shown in (a), along with its profile intensity scan along the blue arrow in (b). A truncated nanoparticle is shown in (c), and its profile intensity scan is shown in (d).

was applied. The simulations combined molecular dynamics with Monte Carlo swaps and were performed using the LAMMPS software[37]. A starting timestep of 1×10^{-5} femtoseconds and a temperature of 10 K were used. Because the starting positions of the atomic species were picked at random, this small timestep was used to avoid the nanoparticle structure deformation. During the simulation, after every 100 MD steps, 100 MC swap attempts were performed for each pair of elemental species (a total of 1×10^6 MC swaps attempts). This approach ensures a comprehensive exploration of possible configurations, driving the system toward the most energetically favorable arrangement. To accept or reject every Monte Carlo swap, the Metropolis-Hastings algorithm was used. A bigger time step (1×10^{-2} fs) and a higher temperature were used when the energy started to converge to a given value. Atomic interactions were modeled using a combination of Embedded Atom Model (EAM)-like potentials (Au-Au, Cu-Cu and Au-Cu[38], Ni-Ni, Pd-Pd and Ni-Pd[39], Au-Ni and Cu-Pd[40], Au-Pd[41], and Cu-Ni[42]). The radial distribution functions were calculated using a home-made code written in Python.

3 Results

3.1 Convergent-Beam Electron Diffraction (CBED) & HOLZ

Most of the AuCuNiPd nanoparticles have shapes with pseudo five-fold symmetry with a regular or irregular shape. The composition of nanoparticles was analyzed by X-ray emission in the TEM (EDS). The results indicate significant differences in concentrations of each nanoparticle. An example of the composition of individual particles is shown in Table 1. One particularly useful technique is the analysis of of Higher-Order Laue Zone (HOLZ)

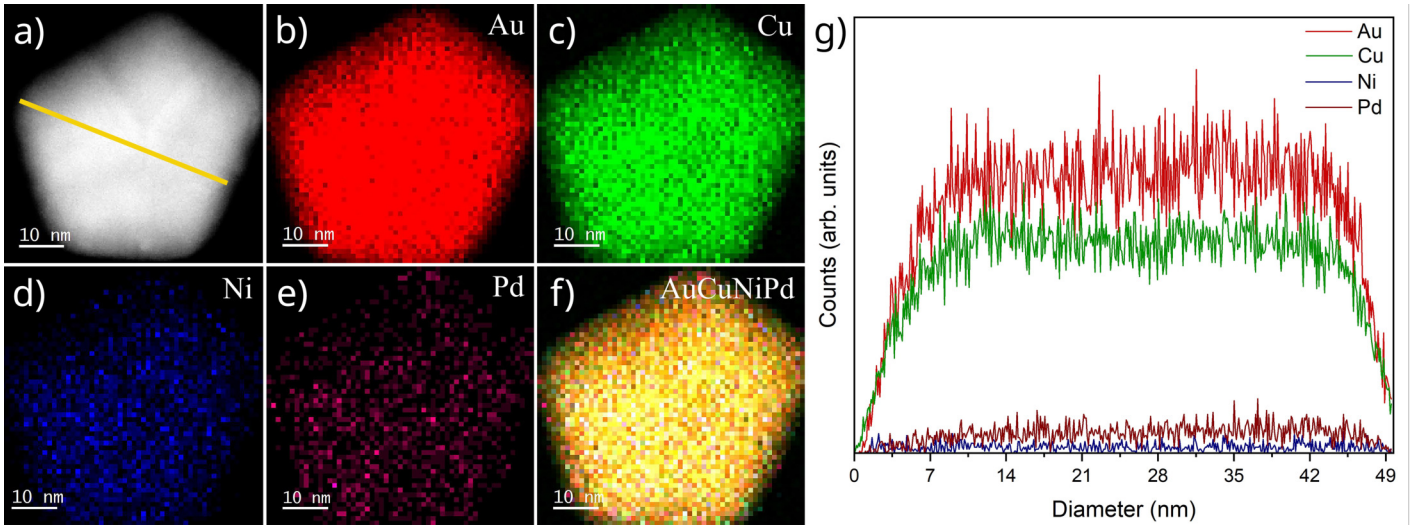

Fig. 2 HAADF-STEM image of decahedral AuCuNiPd nanoparticle (a). EDS mapping showing an evenly distribution of Au (b), Cu (c), Pd (d), and Ni (e) atoms. The contribution of all elements is shown in (f). Au, Cu, Ni and Pd elemental profiles along the yellow line across the pentagonal particles (g).

Chemical element	Sample 1 (%)	Sample 2 (%)	Sample 3 (%)	Sample 4 (%)	Sample 5 (%)	Average of a large area (%)
Ni	2.42	0.18	0.66	0.24	2.2	1.18
Cu	27.5	26.7	27.4	22.3	27.0	27.2
Pd	12.4	16.7	11.9	11.2	2.15	10.2
Au	57.43	56.34	59.9	66.1	68.65	61.4
Total:	99.75	99.92	99.86	99.84	100.0	99.98

Table 1 Elemental distribution measured using energy-dispersive X-ray spectroscopy for five different decahedral nanoparticles and an overall average of a large area containing several nanoparticles.

rings which in conjunction with spot patterns enables a structure to be measured in three dimensions at once as shown in Figure 3.

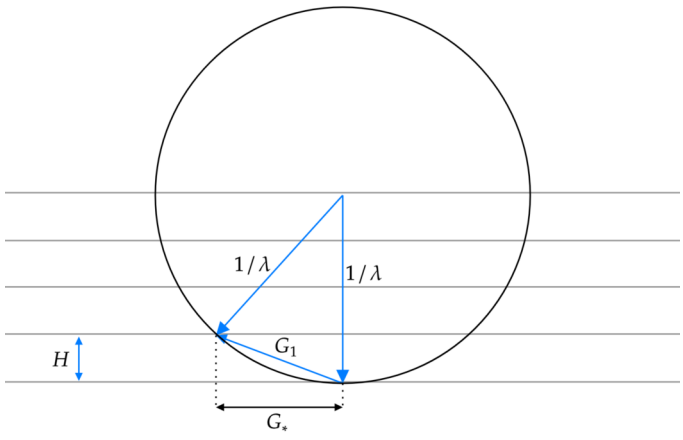

Fig. 3 Ewald sphere construction of HOLZ ring diffraction conditions. For convenience, the array of dots is replaced by a series of lines representing lattice planes.

Using trigonometry the value of H can be obtained. G_1 is the measured radius of the first order HOLZ ring on the diffraction pattern, and λ can be calculated from the accelerating voltage. For 200kV $\lambda \approx 2.5$ pm. The derivation is: $G_* = \sqrt{\frac{2H}{\lambda} + H^2}$ and $G_1^2 = G_*^2 - H^2$, therefore $H = \frac{1}{2}\lambda G_1^2$.

In practical terms we found that almost all samples will create distorted HOLZ rings when tilted slightly off axis. We derived a generalized relationship that exists between the HOLZ ring diameter and the angle by which the sample is tilted away from the zone axis. Once again, the Ewald circle construction simplifies the explanation of this relationship, as shown in Figure 4. For reference, G_{tilt} is the length between the optic center and the zone axis center. Thicker samples will provide some Kikuchi lines to show the location of the zone axis center in many cases. If Kikuchi diffraction is not present, however, it is helpful to consider that both the HOLZ and ZOLZ spots will form arcs, and both arcs will be coaxial about the zone axis. The preferred method of measurement is to create two coaxial circles centered about the Kikuchi indicated zone axis if possible, and if not, they should be centered to best capture the HOLZ and ZOLZ diffraction spots.

This generalized HOLZ ring equation was used to study a multimetallic decahedral nanoparticle of AuCuNiPd. Figure 5 shows a typical pattern obtained in the off-axis configuration, the Zone Axis Pattern (ZAP) center is marked by the intersection of several Kikuchi lines, and coaxial circles are drawn to intersect the ZOLZ and HOLZ arcs.

Circles are used to calculate G_{tilt}, and G_{nz} where $G_{tilt}=r_{ZOLZ}$, and $G_{nz}=r_{HOLZ}-r_{ZOLZ}$. To test of the accuracy of this method several of these patterns were taken at arbitrary tilt angles for a single ZAP. The results of this are shown in Table 2.

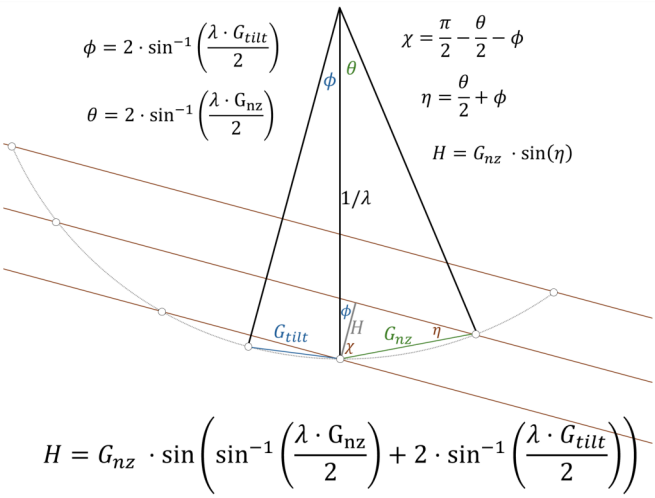

Fig. 4 Ewald representation of generalized HOLZ ring equation indicating a sample tilted away from a zone axis. The lattice distance, H, is given as a function of the distance from the primary beam to the zone axis center (G_{tilt}), the distance from the first HOLZ ring to the primary beam (G_{nz}), and the wavelenght of the beam (λ).

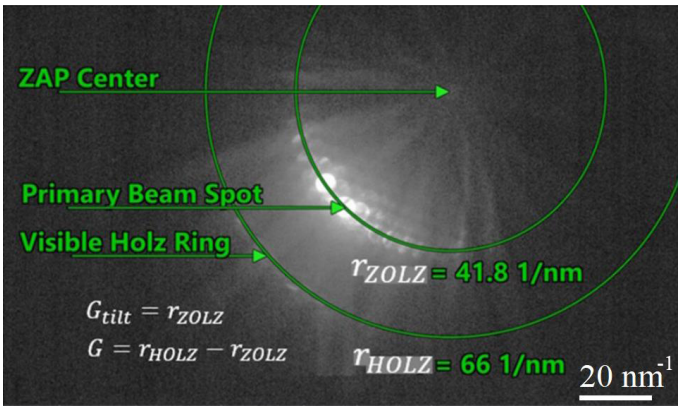

Fig. 5 Demonstration of the generalized HOLZ ring equation on a diffraction pattern of an AuCuNiPd decahedral nanoparticle. Note that in this figure "G" refers to the term "G_{nz}" that is used elsewhere in this text.

The assumed overall distorted Face Centered Cubic lattice, because of the atomic radius differences of the metal elements, results in a Body Centered Tetragonal (BCT) lattice. The consistency in the measurements is very good, and thus for this multimetallic nanoparticle (AuCuNiPd) there is evidence that the lattice is not an overall Face-Centered Cubic (FCC) lattice. To confirm the data and to find an accurate lattice constant, we analyzed a Convergent Beam Electron Diffraction (CBED) pattern with the JEMS software[43]. The result is shown in Figure 6. The pattern can only be fitted with an c/a ratio of 1.45. This result is a BCT lattice with $a = b = 0.287$ nm and $c = 0.4158$ nm. The slight difference between a, b, and the average lattice value obtained in Table 2, 1/H $\approx$ 0.3 nm, likely arises from the different atomic radii of the metals (Au, Cu, Pd, and Ni) used to produce the alloy.

3.2 LACBD measurements

Nanobeam and Selected Area Electron Diffraction (SAED)

Order	G_{tilt} (1/nm)	G_{nz} (1/nm)	H (1/nm)	1/H (nm)
1	31.00	29.06	3.312	0.302
1	41.80	24.20	3.263	0.306
1	56.50	20.10	3.342	0.299
2	56.5	35.90	3.335	0.300

Table 2 Off-Axis HOLZ analysis of four arbitrary tilts, note that the overall variability in the measurement is within seven picometers.

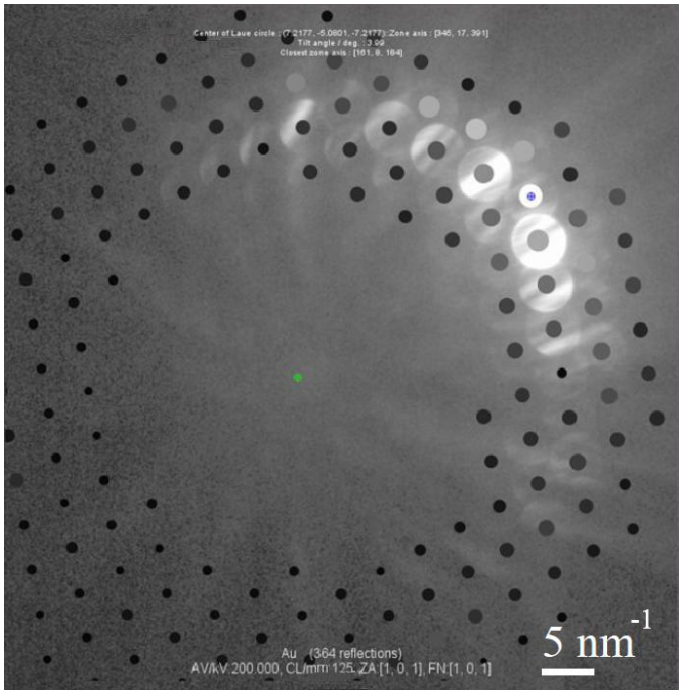

Fig. 6 Fitted diffraction patern of AuCuNiPd decahedral nanoparticle, the standard gold FCC lattice had been distorted by changing the value of c to 4.158 Å indicating a BCT structure.

diffraction patterns are extremely powerful, however, in general they lack 3D information. As shown in Figure 7c and Figure 7d the spots in nanodiffraction are very sharp and they are sensitive to strain but also to the nanoparticle orientation. For this reason, we chose to focus on CBED and LACBED techniques to study multimetallic decahedral particles. Generally, CBED is generated using a focused probe that only excites a very small area of the sample, in the case of the decahedral nanoparticles this would give us roughly the same information as nanobeam diffraction, which is not surprising since nanobeam diffraction is nothing more than CBED with a very small objective aperture. To overcome this, one of two things can be done; the stage can be raised or lowered so that the sample is no longer located at the crossover of the probe, or the objective lens can be adjusted to obtain the same level of defocus. One additional bonus that comes from both methods is that a defocused diffraction pattern will have image information mixed into it. In LACBED Dark field images are also formed in each of the diffracted spots and only the features in the sample that contribute scattering of the disk are illuminated. In Figure 7 we show a typical decahedral MMNP with the TEM image (Figure 7a) and the corresponding FFT showing a pseudo five-fold

symmetry produce by the cyclic twinning, Figure 7b. Then, in Figure 7c and Figure 7d, is shown the LACBED pattern of these AuCuNiPd nanoparticles.

Every spot of Figure 7c represents the dark field image of a tetrahedron forming the decahedra. The central spot is the bright field image[44]. The first row of relaxions correspond to (111) spots and the second to (200) spots. Dark field images are extremely sensitive to strain and thickness variations. In the case of nanoparticles dark field images taken in a condition far from the Bragg conditions is the most accurate method to determine the particle shape[45]. Decahedral nanoparticles tend to have a flat shape as shown by Koga and coworkers[46,47]. As discussed above the AuCuNiPd nanoparticles are rather flat. And since the different metals are distributed along the nanoparticlethe the contrast is mostly due to strain. The brightest areas of the tetrahedra image are close to the center of the decahedra. In other words, the strain is mostly concentrated around the intersection of the five decahedra. In our case the pattern seems to be 2+2+1 meaning that there are two pairs of tetrahedra with similar strain and one with different profile. This is shown in Figure 7c where two sides are marked as A two as B and the single one as C. But it is difficult to say whether this is a real observation or an artifact of zone axis misalignment. To verify the observation several defocussed CBED were analyzed using diffraction disks that were far enough away from the optic axis to prevent overlap. The results are shown in Figure 7.

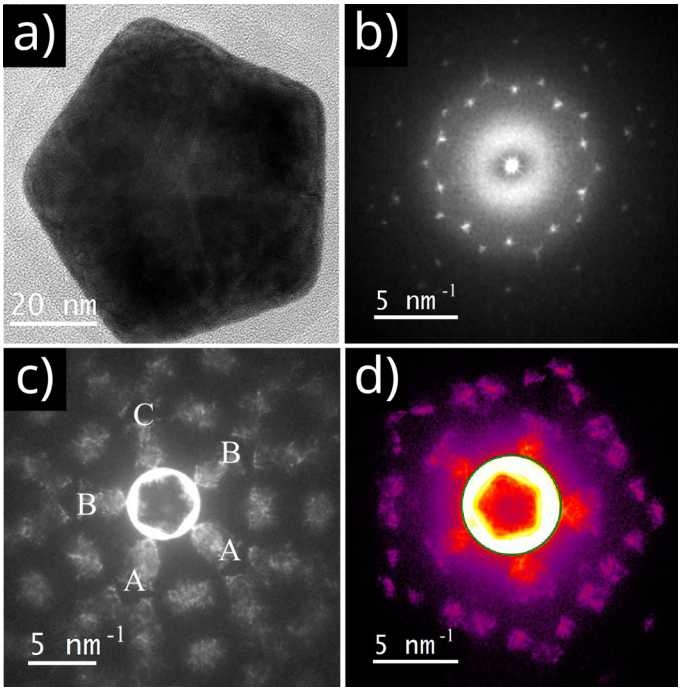

Fig. 7 TEM Image of a decahedral particle (a). FFT of the high-resolution image showing a pseudo five-fold symmetry produce by the cyclic twinning. LACBED of the pentagonal particle (c). LACBED pseudo coloured to show the spots (d).

A very remarkable characteristic of the pattern is that the spots on the (200) ring do not fall in a straight line. This is clearly indication of strain on the nanoparticle. The lattices are consistently distorted, and there appears to be a tendency toward two pairs of facets each having the same spacing while the last one assumes a different value altogether. While this may seem trivial its likely one of the first conclusive measurements of strain in a Dh NP. This is likely because Dh NPs are very difficult to capture in diffraction unless advanced techniques like defocused CBED are used. In order to obtain some quantitative information we have measured the distances of the decahedron array in the (200) ring. We have tabulated the values for all of the measurements in these patterns and the average distortion of these Dh NP's is right at 2.3% which is quite significant, the values are shown in Table 3.

Side	Dh_1 (1/nm)	Dh_2 (1/nm)	Dh_3 (1/nm)
1	17.4	9.89	12.81
2	17.0	9.94	12.78
3	17.1	10.2	12.73
4	16.9	10.1	12.84
5	17.3	10.2	12.85
Distortion	2.9%	3.1%	0.9%
Average distortion			2.3%

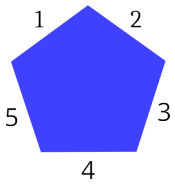

Table 3 Diffraction spots spacing for the analyzed nanoparticles. The values in column "Side" refer to the sides of the tetrahedra forming the decahedron, as illustrated in the figure at the side. The values in each column beginning in "Dh" are the vector lengths. All of these values were obtained from diffraction data and are shown in inverse distance units.

3.3 Theoretical results

Theoretical simulations were performed to explore the atomic structure and chemical order of decahedral nanoparticles. The composition chosen was $Au_{60}Cu_{28}Pd_{10}Ni_2$, which is very close to the average composition found experimentally, and the nanoparticle size investigated was 23.5 nm (169,905 atoms). The metals were put randomly in the chosen proportions and after the elements' chemical order (atomic distribution) was optimized, resulting in a structurally stable configuration. The elemental distribution's homogeneity was confirmed by a simulated line scan through the nanoparticle (Figure 8b), indicating even distribution. This uniformity is crucial for applications where consistent surface or bulk properties are essential, such as catalysis or optical functionality. Figure 8a, shows the calculated *xy* component of the elastic strain, where is clear the random distribution of the lattice deformations, with zones of negative and positive strain very close to each other along the whole nanoparticle. To further analyze the atomic structure, the radial distribution function (RDF) was calculated. The RDF results (Figure 9) strongly suggest a distorted FCC structure, likely influenced by the shape and size of the nanoparticles, alloying effects, and specific proportions of the metals. Distortions in the FCC structure could result from the difference in atomic sizes and bonding preferences of the four constituent metals, which induce local lattice strain. To pinpoint the type of distortion, the nanoparticle RDF was fitted to three candidate distorted lattice structures: face-centered orthorhombic (FCO), base-centered orthorhombic (BCO), and body-centered tetragonal (BCT). Each candidate lattice was mod-

eled using monometallic cells (10x10x10) with initial lattice parameters based on the FCC lattice constant (a=b=c=3.6Å) or plausible distortions (a=b=2.5Å, c=3.6 Å for BCO and BCT).

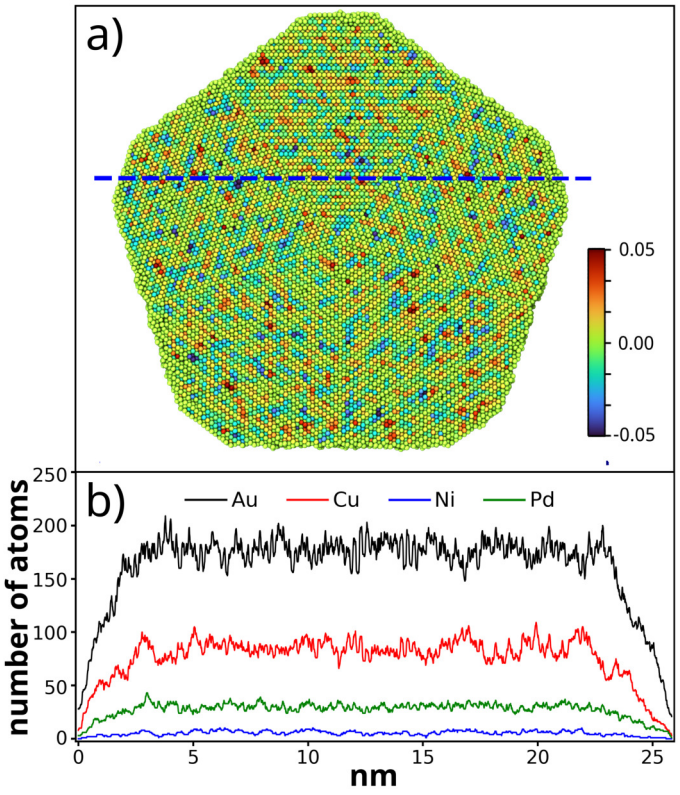

Fig. 8 a) Optimized atomic distribution of the decahedral nanoparticle with a size of 23.5 nm (169,905 atoms) showing the *xy* component of the elastic strain. A random and uniform distribution of the constituent elements (Au, Cu, Pd, Ni) was observed, agreeing with the results reported by Velázquez Salazar *et al.*[32] b) Simulated line scan along the nanoparticle (blue line in Fig. 7a), showing even elemental distribution across the nanoparticle.

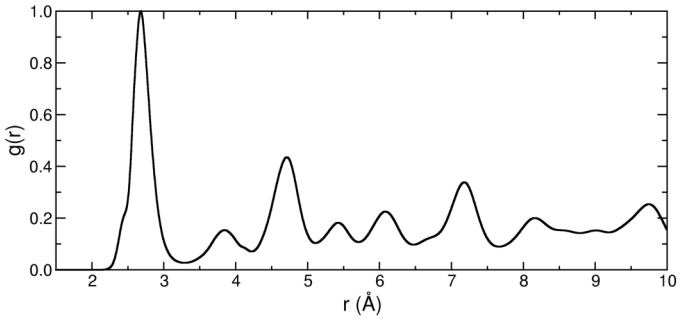

Fig. 9 Radial distribution functions (RDFs) for the 23.5 nm nanoparticle. The results suggest a distorted FCC structure, which is further analyzed by fitting to FCO, BCO, and BCT lattices.

After, the RDF was calculated for each lattice, a Gaussian broadening (sigma=0.1) was applied (to simulate a distribution of distortions around peaks). Once the broadening was applied, the position of the five highest peaks was calculated and compared with the ones corresponding to the nanoparticle. The aforementioned process was converted in an optimization problem using the optimize package of the Scipy Python library and using the Powell's method. The final result for each lattice was:

- FCO: a=3.8467 Å, b=3.8695 Å, c=3.7657 Å,
- BCO: a=2.7534 Å, b=2.6977 Å, c=3.7942 Å,
- BCT: a=2.7015 Å, b=2.7015 Å, c=3.8529 Å.

Figure 10 shows the radial distribution functions resulting from the optimizations. In Figure 10a the optimized RDF without applying the broadening are shown, where is clear by the position and the number of peaks observed that they represent three different lattices. However, when the broadening is applied to the optimized RDF (Figure 10b), they resemble very well the nanoparticle's RDF. A comparative analysis of the fits reveals the following: The BCT lattice provided the best fit, as evidenced by the alignment of peak positions and intensities. This suggests that the nanoparticle's distorted FCC structure is best represented by a BCT configuration. The BCO lattice yielded a slightly poorer fit, though it still provided reasonable agreement, indicating some structural features consistent with orthorhombic distortion. The FCO lattice exhibited the least agreement with the nanoparticle RDF, likely due to its higher symmetry and less flexible parameters. The observation that the BCT structure fits best has significant implications. The preference for this configuration could result from the combined effects of nanoparticle size and shape, and the random distribution of atoms. These factors likely induce specific distortions that stabilize the structure in a BCT-like arrangement, minimizing internal strain while accommodating the alloy's compositional complexity. In conclusion, the RDF analysis provides compelling evidence that the decahedral nanoparticles exhibit a distorted FCC structure best described by a BCT lattice. This insight enhances our understanding of the structural characteristics of multimetallic nanoparticles and lays the groundwork for further studies on their functional properties.

4 Discussion

In this work, we have studied the distortion and strain introduced on a multimetallic AuCuNiPd nanoparticle using CBED methods. We have found that there is a significant strain in the whole particle resulting in an overall departure from the expected FCC lattice. Our results for MMNP seem to be different from those found by Jhonson *et al.* for pure gold[6]. Our results show consistent values for the lattice distortion in both HOZL and LACBD results. However the more reliable were obtained by averaging six particles using both methods. That is a way to improve the accuracy of these two techniques. The most significant point is that our results clearly shown that the structure of the decahedral particles is a distorted FCC. Both kind of techniques yeld to the concusion that the structure is distorted, and that the lattice is best fitted with a BCT structure. The overall lattice matches a BCT structure with a = b = 0.287 nm and c = 0.415 nm. Recent reports in the literature find BCT and BCO lattices in pure gold[48,49] at high pressure and in the form of nanorods[50]. Another report finds orthorhombic lattice under that condition[51]. The internal strain produced by the difference in atomic radius seems to be similar to the effect of high pressure. The images of LACBD are

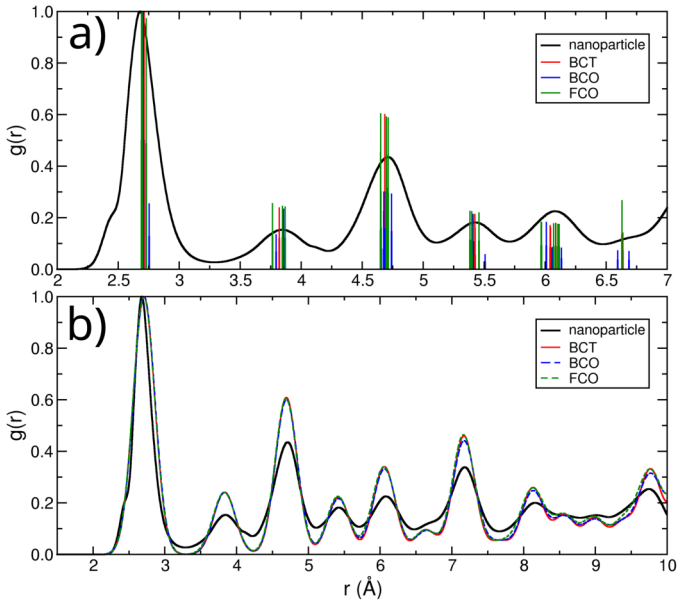

Fig. 10 Radial distribution functions calculated for the optimized FCO, BCO, and BCT lattices before applying Gaussian broadening. The positions and number of peaks highlight clear structural distinctions between the lattices. b) Broadened radial distribution functions of the FCO, BCO, and BCT lattices compared to the nanoparticle RDF. The BCT structure provides the best fitting.

taken with the particle in the Laue condition. Therefore, we expect the same excitation error for each tetrahedron[4,52] and the strain contrast is more ubiquitous in the image. Clearly, the strain is not homogeneous especially near the center of the particle. Velázquez Salazar *et al.* reported strain in decahedral nanoparticles, with the same elements and similar composition to the ones reported in this paper, using HAADF-STEM atomic resolution images[32]. There, we applied the Geometric Phase Analysis method (GPA)[53–55] to determine the spatial distribution of strain (see Fig. 5 in reference[32]). In the present paper, the same information was obtained by a combination of CBED methods, EDS and Molecular Dynamics. As shown in Figure 8a, we obtained a more detailed strain distribution. In particular, we noted that in the center of the particle there is increased strain. This is most likely due that the fact that in the center five twin boundaries meet. This is expected because in addition to the strain due to different atomic radius, there is strain due to the fact that strain is necessary to close the gap produced in a decahedral structure by packing five regular tetrahedra[56]. We conclude that CBED methods can give more accurate values for the lattice parameters. The Molecular Dynamics can give us deeper insights about the spatial strain distribution. Nevertheless, the result is that the overall particle can be described by a non-FCC lattice. However, theoretical analysis suggests that either BCT, FCO and BCT lattices are equally fitting the distortion with a very slight preference for BCT.

It is also very interesting that in MMNP with high content of gold, the predominant shapes present five-fold symmetry such as dechahedra and icosahedra, sometimes regular and sometimes irregular. In recent works by the group of Ferrando and coworkers[57–59], they found that in the case of alloy bimetallic nanoparticles (AuCu) the icosahedral packing is very likely. That includes several types of geometries, being chiral and non-chiral, including capped icosahedra, as well as the truncated decahedron, a five-fold structure whith in the nanoparticle growth process, is on the growth path from the decahedra to the icosahedra[60]. Here we consider that at the beginning of the growth process, clusters of icosahedral-decahedral shape are formed predominantly. However, the growth process is dominated by the kinetics that frozen the five-fold structures. When more atoms are incorporated to the cluster, the kinetics most likely takes over and the five-fold shape freezes. As more atoms arrive to the growing particle they add to the five-fold structure but do not necessary reach equilibrium lattice sites. The result are shapes close to the decahedron, capped icosahedron and irregular shapes with a fivefold core. In nanoalloys, the misfit strain creates a dynamic interplay between stress accumulation and geometric evolution in core@shell nanoparticles, guiding the formation of various morphologies based on the initial structural configurations and compositions of the seeds, as has been previously reported[61]. The fact that there are different types of fivefold shapes present, including irregular ones, confirms the role of kinetics.

5 Conclusions

Electron diffraction using HOLZ patterns and LACBED is a key method to study multimetallic alloys. We have reported a new method to analyze asymmetrical HOLZ patterns, which results in accurate lattice spacing determinations. Our work reported AuCuNiPd nanoparticles. Multimetallic nanoparticles preferentially produces decahedral structures, including regular and irregular shapes, which are distorted with respect to the FCC lattice. This results can be fitted to a BCT lattice with a=b=0.287 nm and c=0.415 nm. However, it can equally be fitted to a BCO or FCO. The differences are very small, however the CBED results favors the BCT structure. This only refers to an average lattice. It should be remarked that if we analyzed individual tetrahedra by LACBED, we find significant differences between them. It seems that the strain comes in two pairs of tetrahedra, each with a different strain and a fifth one with a different strain from the others. This model that can be named 2+2+1 will be discussed in a forthcoming publication. Our methods provide, very useful information about the strain distribution in very large particles. Our results proved that the multimetallic alloys show a distorted crystal structure. We believe that our particles are large and they also are a model to study advanced bulk alloys such as Heusler alloys, high entropy alloys and many others. This open the way to the understanding of their properties.

Author contributions

Blake Rogers: investigation, formal analysis, TEM images. **Carlos E. Rufino da Silva:** writing– review & editing, visualization. **Juan Pedro Palomares-Báez:** MD Simulations, writing– review & editing, formal analysis. **J. Jesús Velázquez Salazar:** Chemical synthesis, writing– review & editing. **José Luis Rodríguez López:** writing– review & editing. **Juan Martín Montejano-Carrizales:** writing– review & editing. **Miguel José Yacamán:** writing– original draft, writing– review & editing, investigation, formal analy-

sis, coordination, supervision, conceptualization.

Conflicts of interest

There are no conflicts to declare.

Data availability

Data will be made available under request.

Acknowledgements

The authors acknowledge: The support of the Department of Energy (DOE) grant Mission DAC: Molecular Mechanisms of Moisture Driven DAC with Charged Polymers. The Foundational Research for Electronic Warfare in Multi-domain Operations (FREEDOM) Essential Research Program (ERP). The Nanotechnology Collaborative Infrastructure Southwest (NNCI-SW). The Center for Materials Interfaces in Research & Applications (¡MIRA!) at Northern Arizona University (NAU) for allowing them to use its facilities. The LANCAD and CONAHCYT for the granted computing time on the supercomputer Miztli at DGTIC, UNAM.

Notes and references

1 S. Ino, *Journal of the Physical Society of Japan*, 1966, **21**, 346–362.
2 M. Yacaman, K. Heinemann, C. Yang and H. Poppa, *Journal of crystal growth*, 1979, **47**, 187–195.
3 C. Y. Yang, *Journal of Crystal Growth*, 1979, **47**, 274–282.
4 L. Marks, *Surface Science*, 1985, **150**, 302–318.
5 L. Marks and L. Peng, *Journal of Physics: Condensed Matter*, 2016, **28**, 053001.
6 C. L. Johnson, E. Snoeck, M. Ezcurdia, B. Rodríguez-González, I. Pastoriza-Santos, L. M. Liz-Marzán and M. J. Hÿtch, *Nature Materials*, 2008, **7**, 120–124.
7 M. Hÿtch and P. W. Hawkes, *Quantitative atomic-resolution electron microscopy*, Academic Press, 2021.
8 B. S. Murty, J.-W. Yeh, S. Ranganathan and P. P. Bhattacharjee, *High-Entropy Alloys*, Elsevier, 2014.
9 E. P. George, D. Raabe and R. O. Ritchie, *Nature Reviews Materials*, 2019, **4**, 515–534.
10 V. G. de Paula and M. S. Reis, *Chemistry of Materials*, 2021, **33**, 5483–5495.
11 T. Kojima, S. Kameoka and A.-P. Tsai, *Science and Technology of Advanced Materials*, 2019, **20**, 445–455.
12 S. Tavares, K. Yang and M. A. Meyers, *Progress in Materials Science*, 2023, **132**, 101017.
13 W. Steurer, *Acta Crystallographica Section A: Foundations and Advances*, 2018, **74**, 1–11.
14 A. P. Tsai, *Science and Technology of Advanced Materials*, 2008, **9**, 013008.
15 L. Wei, E. H. Ang, Y. Yang, Y. Qin, Y. Zhang, M. Ye, Q. Liu and C. C. Li, *Journal of Power Sources*, 2020, **477**, 228696.
16 D. B. Miracle and O. N. Senkov, *Acta Materialia*, 2017, **122**, 448–511.
17 A. Kumar, A. Arora, R. Chandrakar, K. R. Rao and M. Chopkar, *Materials Today: Proceedings*, 2020, **27**, 1310–1314.
18 J. H. Sinfelt, *Chemistry and Industry*, 1984, 403–6.
19 J. Wang, H. Chen, Z. Hu, M. Yao and Y. Li, *Catalysis Reviews*, 2015, **57**, 79–144.
20 D. Nelli, C. Roncaglia and C. Minnai, *Advances in Physics: X*, 2023, **8**, 2127330.
21 D. Cherns, *Le Journal de Physique IV*, 1993, **3**, C7–2113.
22 J. Zuo, R. Holmestad, J. Spence and R. Høier, Microbeam Analysis, 1995: Proceedings of the 29th Annual Conference of the Microbeam Analysis Society, 1995, p. 269.
23 G. Brunetti, A. Settefrati, A. Hazotte, S. Denis, J.-J. Fundenberger, A. Tidu and E. Bouzy, *Micron*, 2012, **43**, 396–406.
24 L. Clement, F. Cacho, R. Pantel and J.-L. Rouviere, *Micron*, 2009, **40**, 886–893.
25 A. Armigliato, R. Balboni and S. Frabboni, *The European Physical Journal-Applied Physics*, 2004, **27**, 49–54.
26 A. Armigliato, A. Spessot, R. Balboni, A. Benedetti, G. Carnevale, S. Frabboni, G. Mastracchio and G. Pavia, *Journal of Applied Physics*, 2006, **99**, year.
27 C. Chou, S. Anderson, D. Cockayne, A. Sikorski and M. Vaughan, *Ultramicroscopy*, 1994, **55**, 334–347.
28 H. Heinrich, A. Vananti and G. Kostorz, *Materials Science and Engineering: A*, 2001, **319**, 434–438.
29 D. Farkas and A. Caro, *Journal of Materials Research*, 2018, **33**, 3218–3225.
30 L. R. Owen and N. G. Jones, *Journal of Materials Research*, 2018, **33**, 2954–2969.
31 G. Casillas, J. P. Palomares-Baez, J. L. Rodriguez-Lopez, J. Luo, A. Ponce, R. Esparza, J. J. Velazquez-Salazar, A. Hurtado-Macias, J. Gonzalez-Hernandez and M. Jose-Yacaman, *Philosophical Magazine*, 2012, **92**, 4437–4453.
32 J. J. Velázquez Salazar, D. Bahena Uribe, J. P. Palomares-Báez, C. E. Rufino da Silva, J. L. Rodríguez López, J. M. Montejano-Carrizales and M. J. Yacamán, *The Journal of Physical Chemistry C*, 2024, **128**, 21836–21845.
33 M. Tanaka and K. Tsuda, *Journal of Electron Microscopy*, 2011, **60**, S245–S267.
34 P. Jones, G. Rackham and J. W. Steeds, *Proceedings of the Royal Society of London. A. Mathematical and Physical Sciences*, 1977, **354**, 197–222.
35 T. Okuyama, S. Matsumura, Y. Tomokiyo, N. Kuwano and K. Oki, *ISIJ International*, 1989, **29**, 191–197.
36 P. Champness, *Mineralogical Magazine*, 1987, **51**, 33–48.
37 S. Plimpton, *Journal of Computational Physics*, 1995, **117**, 1–19.
38 J.-Q. Goh, J. Akola and R. Ferrando, *The Journal of Physical Chemistry C*, 2017, **121**, 10809–10816.
39 Y. Xu, G. Wang, P. Qian and Y. Su, *Journal of Materials Science*, 2022, **57**, 7384–7399.
40 X. Zhou, R. Johnson and H. Wadley, *Physical Review B*, 2004, **69**, 144113.
41 F. Pittaway, L. O. Paz-Borbón, R. L. Johnston, H. Arslan, R. Ferrando, C. Mottet, G. Barcaro and A. Fortunelli, *The Journal of Physical Chemistry C*, 2009, **113**, 9141–9152.
42 E. Panizon, J. A. Olmos-Asar, M. Peressi and R. Ferrando, *Phys-*

ical Chemistry Chemical Physics, 2015, **17**, 28068–28075.
43 *jems-swiss*, `https://www.jems-swiss.ch/`, Accessed: 2025-01-07.
44 D. B. W. C. B. Carter, *Transmission electron microscopy A textbook for materials science*, 2009.
45 M. José-Yacamán and M. Avalos-Borja, *Catalysis Reviews*, 1992, **34**, 55–127.
46 K. Koga, *Physical Review Letters*, 2006, **96**, 115501.
47 K. Koga and K.-i. Sugawara, *Surface Science*, 2003, **529**, 23–35.
48 G. Mettela, N. Mammen, J. Joardar, S. Narasimhan and G. U. Kulkarni, *Nano Research*, 2017, **10**, 2271–2279.
49 G. Mettela, Y. A. Sorb, A. Shukla, C. Bellin, V. Svitlyk, M. Mezouar, C. Narayana and G. U. Kulkarni, *Chemistry of Materials*, 2017, **29**, 1485–1489.
50 Y. Zhou and K. A. Fichthorn, *The Journal of Physical Chemistry C*, 2014, **118**, 18746–18755.
51 R. Mendoza-Cruz, P. Parajuli, H. J. Ojeda-Galván, Á. G. Rodríguez, H. R. Navarro-Contreras, J. J. Velázquez-Salazar, L. Bazán-Díaz and M. José-Yacamán, *CrystEngComm*, 2019, **21**, 3451–3459.
52 M. J. Yacamán and T. Ocaña Z, *Applied Physics Letters*, 1977, **30**, 359–360.
53 M. Hÿtch, A. Lubk, C. Gatel and E. Snoeck, *Acta Cryst*, 2011, **67**, C106–C107.
54 M. J. Hÿtch and A. M. Minor, *MRS bulletin*, 2014, **39**, 138–146.
55 M. Hÿtch, E. Snoeck and R. Kilaas, *Ultramicroscopy*, 1998, **74**, 131–146.
56 B. Rogers, A. Lehr, J. J. Velázquez-Salazar, R. Whetten, R. Mendoza-Cruz, L. Bazan-Diaz, D. Bahena-Uribe and M. José Yacaman, *Crystal Research and Technology*, 2023, **58**, 2200259.
57 R. Ferrando, *Frontiers of nanoscience*, Elsevier, 2022, vol. 21, pp. 71–91.
58 D. Bochicchio and R. Ferrando, *Nano letters*, 2010, **10**, 4211–4216.
59 D. Rapetti and R. Ferrando, *Journal of Alloys and Compounds*, 2019, **779**, 582–589.
60 J. P. Palomares-Báez, J. M. Montejano-Carrizales, G. Guisbiers, M. José-Yacamán and J. L. Rodríguez-López, *Nanotechnology*, 2019, **30**, 425701.
61 R. Ferrando *et al.*, *Nanoscale*, 2023, **15**, 2384–2393.

Data availability statement

Data will be made available under request.